Birkbeck
UNIVERSITY OF LONDON

# BIROn - Birkbeck Institutional Research Online

Yu, W. and Wei, W. and Hammond, James O.S. and Han, C. and Xu, J. and Tan, H. and Zhan, Y. and Yang, Y. (2025) Evidence for an Upper Crustal Melt Lens beneath Tianchi (Changbaishan) Volcano. Journal of Geophysical Research: Solid Earth 130 (1), ISSN 0148-0227.

Downloaded from: https://eprints.bbk.ac.uk/id/eprint/54864/

*Usage Guidelines:*
Please refer to usage guidelines at https://eprints.bbk.ac.uk/policies.html or alternatively contact lib-eprints@bbk.ac.uk.

# Evidence for an upper crustal melt lens beneath Tianchi (Changbaishan) Volcano

**Weiqian Yu[1,2,3], Wei Wei[1†], James O.S. Hammond[3], Cunrui Han[3], Jiandong Xu[2], He Tan[1], Yan Zhan[1] and Yanming Yang[1,4]**

[1]State Key Laboratory of Earthquake Dynamics, Institute of Geology, China Earthquake Administration (CEA), Beijing 100029, China
[2]Jilin Changbaishan Volcano National Observation and Research Station, , Institute of Geology, CEA, Beijing 100029, China
[3]School of Natural Sciences, Birkbeck, University of London, London WC1E 7HX, UK
[4]Earthquake Agency of Inner Mongolia Autonomous Region, 80 Zhelimu Road, Hohhot 010010, China

Corresponding author: Wei Wei (weiwei@ies.ac.cn)

## Key Points:

- A new high resolution 3D Vs model for the crust and uppermost mantle beneath the Tianchi (Changbaishan) Volcano
- Seismic identification of 2 separate low velocity anomalies in the upper crust beneath the Tianchi (Changbaishan) Volcano
- Reactive transport of evolved melts forms an upper crustal melt lens overlying a chemically differentiated, faster lower crust.

## Abstract

Changbaishan volcanic field (CBVF) located on the border of China and the Democratic People's Republic of Korea (DPRK) is famous for intense volcanism in the Cenozoic. Many studies show evidence for partial melt beneath the volcano, but details on the structure of the magmatic system are lacking, due to a lack of data in the region. In this study, we obtained a high-resolution crust and upper mantle shear wave velocity (Vs) model beneath the CBVF by ambient noise tomography and receiver functions using a new dense seismic array. The absence of velocity anomalies beneath Wangtian'e and Namphothe volcanoes suggest a lack of magma within the crust. However, our models reveal two low Vs anomalies below the Tianchi volcano associated with magma reservoirs. The shallow low velocity anomaly (<4 km) overlaps with petrological estimates of the assembly depth of erupted rhyolite magma reservoir and the depth inferred for a hydrothermal reservoir from a recent MT study. The deeper one is located between 7 and 14 km depth with a lateral extent of ~ 30 km, with a melt fraction of ~ 6%-12%. Underlying the deeper low velocity zone in the lower crust is a region of faster velocity compared to the surrounding region. We interpret this as a low melt fraction crystal mush.

## Plain Language Summary

Changbaishan volcanic field (CBVF) is a key area to study intraplate stratovolcanoes. It contains three similar large volcanoes (Wangtian'e, Namphothe and Tianchi) and over 200 smaller volcanoes. The detailed study of the crust and upper mantle structures using geophysics is a direct way to unravel the processes of magma storage and evolution in the region. In this study, we use data from a new dense deployment of seismometers to produce a detailed shear wave velocity model beneath the CBVF. Our models reveal two significant low shear wave anomalies beneath Tianchi volcano (TCV), overlying a faster shear wave velocity lower crust. In the shallow crust (<4 km), the low velocities are associated with fluid and magma. Another low velocity anomaly is located between 7 and 14 km depth with a lateral extent of ~ 30 km, with a melt fraction of ~ 6%-12%. This is likely the main magma reservoir in the upper crust. Our Vs model also shows low velocities in the uppermost mantle beneath TCV, which is a source of partial melt that supplies the volcano. All of this shows that the activity of TCV has not weakened, and there remains the possibility of a future eruption.

## 1 Introduction

Changbaishan volcanic field (CBVF) is an intraplate stratovolcano located ~1400 km away from the Japan trench (Figure 1a). It primarily consists of three calderas named Tianchi (TCV), Wangtian'e (WTE) and Namphothe (NPT) (located in the Democratic People's Republic of Korea (DPRK)) (Figure 1b; Fan et al., 2007; Liu et al., 2015). Among them, TCV is an activate volcano, known for the 'Millennium Eruption', dated to 946 CE (Xu et al., 2013; Oppenheimer et al., 2017) and is often named Changbaishan (or Mount Paektu/Baekdu in Korean). Here we refer to it as TCV to distinguish the specific volcano from the wider CBVF region. Volcanic ash from the 946 CE eruption has been recorded in the ice cores of Greenland (Sun et al., 2014) showing this volcano has the potential for large eruptions and, while debated (Pan et al., 2017), the most recent eruption of TCV was reportedly in 1903 (Xu et al., 2012; Wei et al., 2013). More recently, observations of volcanic earthquakes, ground uplift and hot spring gas activity show that its activity has not weakened, and there remains the possibility of a future eruption (Wu et al., 2005; Liu et al., 2011; Xu et al., 2012).

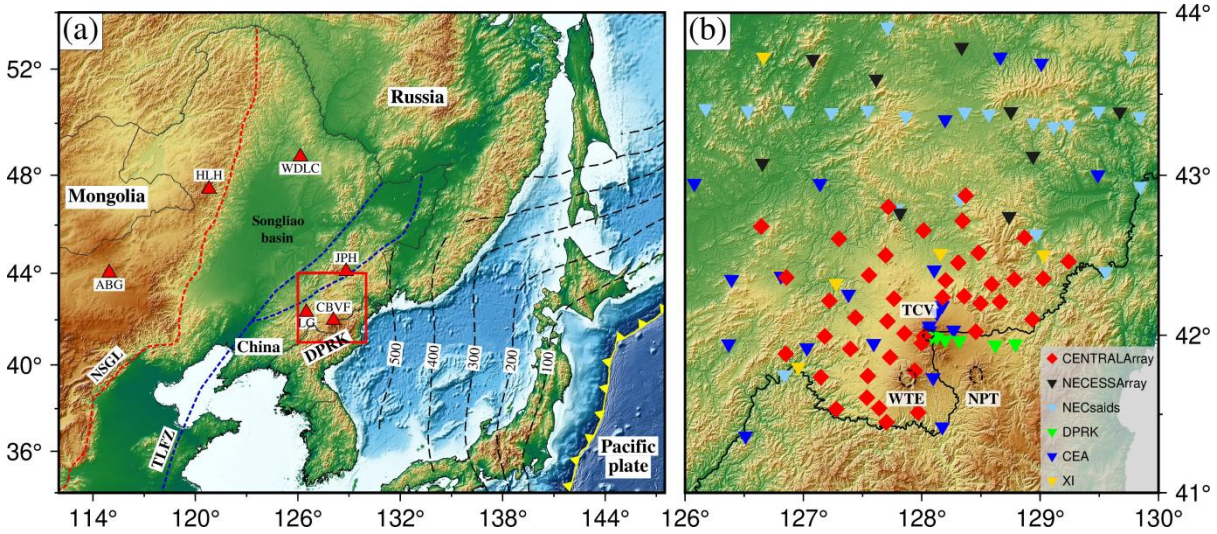

**Figure 1**

The location of CBVF is far from any plate boundary, providing us a good change to investigate the origin and magma evolution of stratovolcanoes in an intraplate tectonic setting. Numerous large-scale seismic tomographic studies have been carried out to better understand this. Some studies suggest that CBVF is associated with hot and wet upwellings in a big mantle wedge above the stagnant Pacific slab in the mantle transition zone (e.g. Lei and Zhao, 2005; Zhao et al., 2009; Wei et al., 2012). However, others propose a more local source, where hot upwelling of sub-slab materials through a gap in the stagnant slab (Tang et al., 2014) or localized release of water (Zhao and Tian, 2013) drive volcanism, results consistent with localized vertical flow in the mantle (Han et al, 2024).

Many studies have attempted to study the magmatic system of CBVF using geophysics, with a wide variety of results (Figure 2). For example, Kim et al. (2017) used ambient noise to obtain a relatively high Vs structure at depths of 15-40 km beneath the CBVF, which they explained as frozen magmatic structures, with no large-scale partial melting in the middle and lower crust beneath the CBVF. However, recent tomographic studies suggest that there is a significant low Vs anomaly in the crust beneath the CBVF (Fan and Chen, 2019; Zhu et al., 2019; Fan et al., 2021, 2022; Li et al., 2023), suggesting the opposite. To the depth, geometry and size of the magma chamber, consistent results have not yet been achieved and different models vary considerably. A low-Vs ellipsoid-like body at 20-35 km depth was revealed by ambient noise adjoint tomography, which was regarded as the presence of a lower-crustal mush zone (Fan et al., 2022). By joint inversion of ambient noise and receiver functions (RFs), Zhu et al. (2019) imaged a low-velocity body at depths of 8-15 km directly beneath the CBVF with a lateral extent of ~100 km in the north-south direction, which was interpreted as a magma chamber in the middle crust, a result similar to that proposed by receiver function studies, which saw the top of a low velocity layer at similar depths (Hammond et al., 2020) extending ~ 20 km laterally. Recent local tomography shows there is a high Vp/Vs ratio at 5 km depth beneath the CBVF, and the dominant anomaly with a value as high as 2.0 is distributed slightly east of TCV, which is deemed as a shallow magma reservoir (Yan et al., 2023). Though some geophysical studies have suggested the existence of multi-level magma chambers beneath the TCV (e.g., Zhang et al., 2002; Yan et al., 2023), there are obviously difference for the locations and scales of the magma reservoirs between models. Petrology on the other hand, provides evidence for magma storage in the upper crust only, supporting models with an absence of melt storage in the deeper crust (Figure 2).

A reason for the lack of clarity in the geophysics is the location of the volcanic region on the border of China and the DPRK. This means that CBVF is always located at the edge of any seismic array (e.g., Guo et al., 2015b; Kim et al., 2017; Zhu et al., 2019; Fan et al., 2021; Li et al., 2023) and so resolution is limited. In this study we deployed a dense temporary seismic network for 3-years named CENTRALArray. The 42 broadband seismometer network, centered on TCV and WTE with a station spacing of 25 km (Figure 1b) allows us to image at much higher resolution throughout the crust. We also include data from the permanent seismic stations of the China Earthquake Administration (CEA), the temporary network of

NECESSArray (NorthEast China Extended Seismic Array) and recent deployments in the DPRK (Mount Paektu Research Centre, 2013).

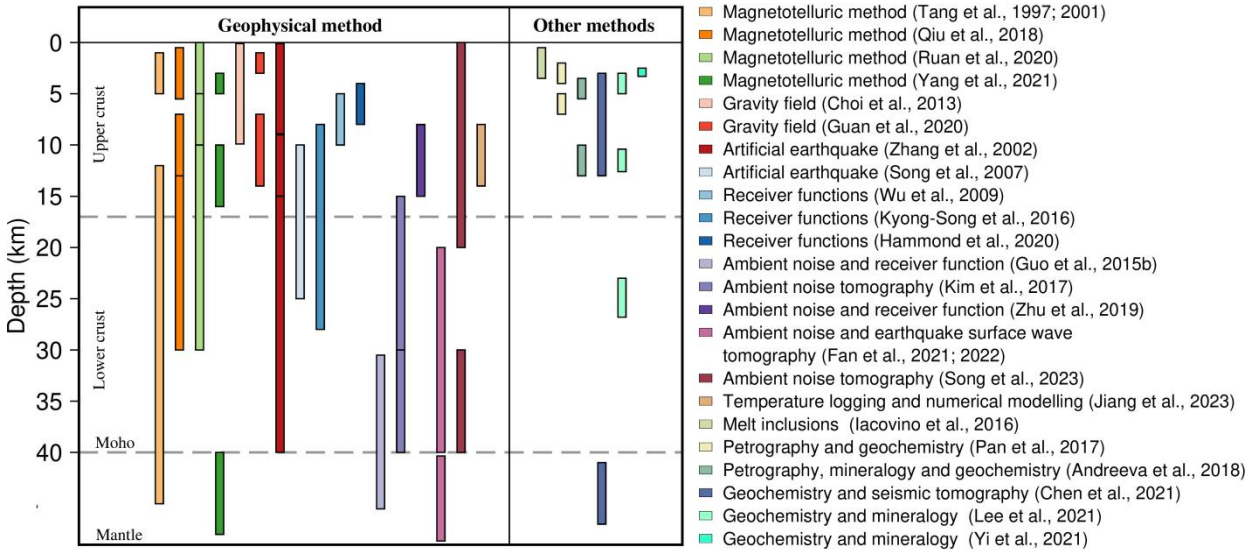


**Figure 2**

## 2 Data and Methods

In this study, we used new seismic data from CENTRALArray (detailed information about deployment periods and station locations are listed in Table S1 and S2) deployed in September 2020 by the Institute of Geology, CEA (Figure 1b). Each station consisted of a Guralp CMG-3ESP or CMG-3ESPC seismometer and a Reftek 130 data acquisition system. In addition, we collected continuous seismic noise records from 2 portable arrays and 1 permanent networks, including 9 NECESSArray portable stations, 6 stations in DPRK and 21 CEA permanent stations. We also used some Rayleigh wave dispersion data provided by Fan et al. (2021). We use ambient noise tomography (ANT) and RFs to image the crustal and uppermost mantle structure beneath the CBVF.

### 2.1 Receiver functions

We used the waveforms from 2086 earthquakes with magnitude ≥ 5.5 and epicentral distances between 30° and 90° (Figure S1) recorded at 78 stations from four networks (Table S1) to obtain reliable RFs. We followed the procedure of Xu et al. (2018) to calculate the RFs. First, we removed the mean shift and linear trend and filtered with a band-pass filter of 0.02-2 Hz. Then, we rotated the E-N components to T-R components. We calculated the signal-to-noise ratios (SNR) and removed SNR < 7 dB. The SNR is calculated by:

$$\mathrm{SNR} = 10 \log_{10} \left( \frac{A_S}{A_N} \right)^2, \quad (1)$$

where $A_N$ and $A_S$ are root mean squares (RMS) of the amplitudes in a 100 s time-window before and after theoretical P arrival times calculated by the Taup toolkit (Crotwell et al., 1999), respectively. We cut the waveforms from 10 s before the theoretical P arrival time

to 120 s after the arrival and calculated the RFs using an iterative time-domain deconvolution method (Ligorría and Ammon, 1999). We set the Gaussian parameter to 2 for each event, which acts as a low pass fillter with cut off of ~ 1 Hz. We manually checked all RFs at each station, and removed RFs lacking a clear Ps conversion from the Moho. We stacked all the RFs at each station after the move-out correction with a reference ray parameter of 0.06 s/km to strengthen the amplitude of the conversion phases (Figure S2).

### 2.2 Ambient noise tomography

For the Ambient noise tomography, we followed the procedures described by Bensen et al. (2007) to compute inter-station empirical Green's functions (EGFs) from the cross-correlation functions (CCFs) across all networks. The vertical components of ambient noise data were cut into 1 day segments and decimated to 5 Hz. After removing the mean, trend and instrument response, all records were band-pass filtered between 1s and 50 s. We applied spectrum whitening and normalization of the waveform and finally, we calculated CCFs for the vertical components of all station pairs. We stacked all CCFs for each station pair and added the positive and negative parts of the CCFs to enhance the SNR and reduce the effect of the heterogeneous distribution of the sources. Each folded and stacked CCF converged towards the estimated EGF between each pair of stations. Figure 3 shows the resulting CCFs filtered at different bandwidths based on the inter-station distance.

We obtained the Rayleigh phase velocity dispersion curves using a frequency-time analysis (FTAN; Levshin and Ritzwoller, 2001). We also include some dispersion curves from Fan et al. (2021) with NECsaids (NorthEast China seismic array) and XI (PASSCAL-XI) portable stations in our study region to increase the ray coverage of the middle-lower crust. Details related to the CCFs calculated, stacked and dispersion measurements can be found in Text S1 and Figure S3 in the supporting information. To ensure that only reliable measurements of phase velocities are used for ANT, three quality criteria have been applied: 1) the SNR as defined in Bensen et al. (2007) must be larger than 10; 2) the separation of the stations must be larger than 1.5 wavelengths; 3) Rayleigh wave dispersion curves must be clear and continuous. After this quality control, we obtained 2229 dispersion curves. Figure S4 show some examples of dispersion curves. The number of dispersion curves for each period is shown in Figure S4c.

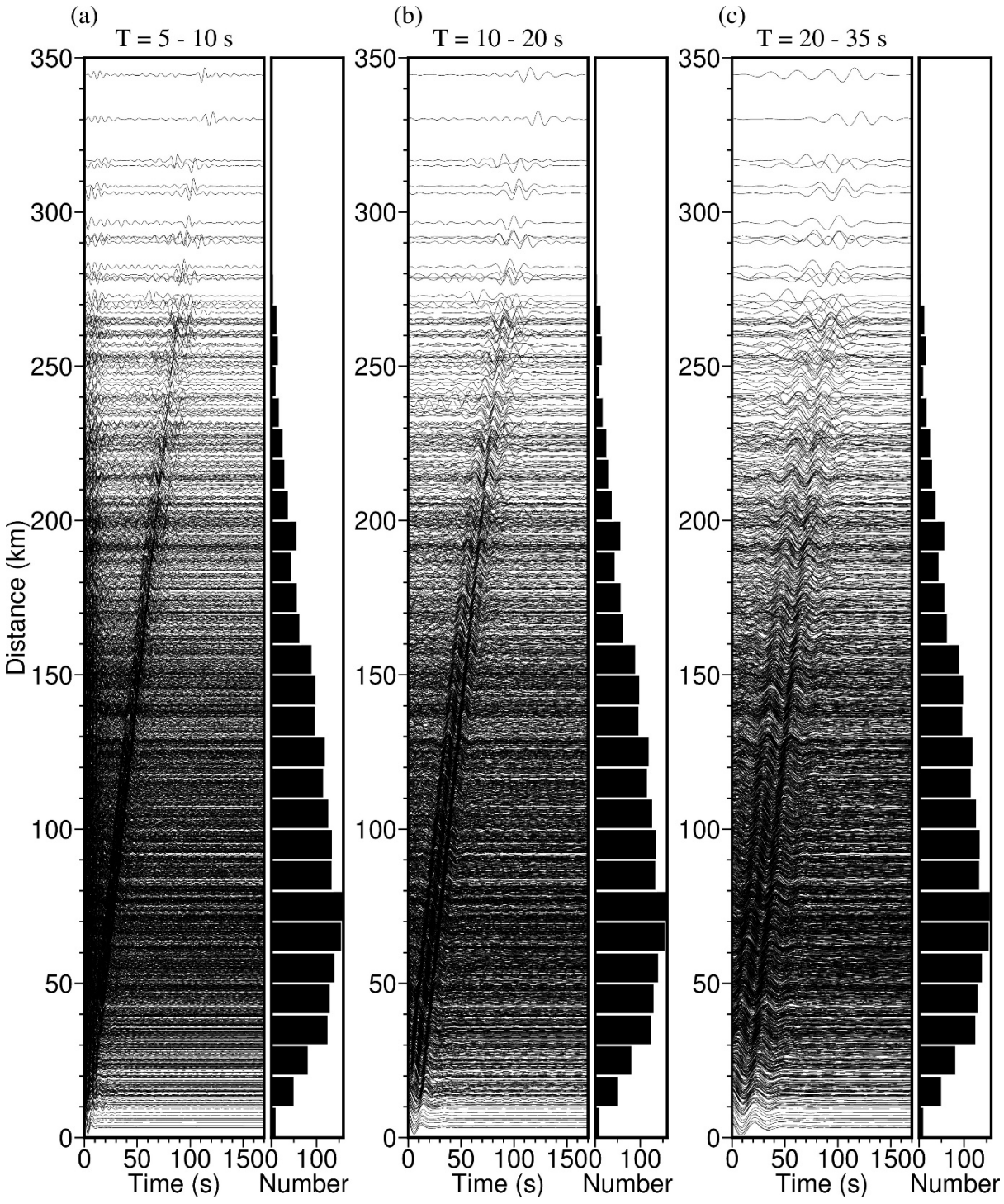


**Figure 3**

The inter-station phase velocity measurements were inverted for 2D Rayleigh wave phase velocity anomaly maps at 2-37 s periods using the Fast Marching Surface Tomography (FMST) described in Rawlinson and Sambridge (2005). FMST is an iterative nonlinear tomographic method, which is based on the Fast Marching Method (FMM) and subspace inversion algorithm (Sethian, 1996; Rawlinson and Sambridge, 2005). The study area (Figure 1b) is parameterized with a lateral grid interval of 0.1°. We investigate the trade-off curves between data variance and model roughness to determine the most appropriate damping and smoothing

values in the inversion process (red square in Figure S5). Based on local dispersion curves, an iterative linearized inversion algorithm of Herrmann (2013) is employed to invert for 1D Vs models. The study region is parameterized into 1271 grid points ($0.1° \times 0.1°$) and a 3D Vs model is generated by combining the 1D Vs models. The initial model for each grid is interpolated from the study of Shen et al. (2016). The thickness of each layer is 1 km at depths above 10 km. At depths of 10 to 40 km, the thickness is 2 km per layer. And at the depths of 40 to 80 km, the thickness increases to 5 km per layer. Only shear wave velocity was inverted for due to the primary sensitivity of Rayleigh wave dispersion to S-wave velocities. The P-wave velocities and density in each layer were estimated by S-wave velocities from empirical relationships (Brocher, 2005).

### 2.3 Joint Inversion

Ambient noise tomography is sensitive to absolute Vs and provides spatially coherent velocity models, but it is less sensitive to velocity discontinuities. In contrast, P wave receiver functions can constrain discontinuity structure well, but are less sensitive to the absolute Vs structure. Jointly inverting for these datasets has been shown to be effective at constraining both (Julia et al., 2000).

We used a linearized inversion method (Herrmann, 2013) to jointly invert RFs and ANT at each seismic station to obtain a 1D Vs model. From the phase velocity tomography, we obtained dispersion curves with a grid size of $0.1° \times 0.1°$. However, the location of RFs data is constrained by seismic station locations rather than grid points. Thus, we search the closest dispersion curves to the seismic station for the joint inversion. In this work, we set the initial model to be the same as the ANT in the joint inversion, and use a weighting factor of 0.2, indicating $20\%$ weight on the dispersion data and $80\%$ on the RFs.

## 3 Results

### 3.1 Checkboard tests

To evaluate the resolution of our phase velocity models, we performed checkboard tests for anomaly sizes of $0.2° \times 0.2°$ and $0.3° \times 0.3°$ (Figures 4 and S4) with $\pm 0.3\,\mathrm{km/s}$ velocity perturbations of the average velocity for each period. Gaussian noise with a standard deviation of 0.3s was added to the synthetic phase travel time. Finally, we performed checkboard tests by using the same ray path distribution and parameters as the real inversion. As shown in Figures 4 and S4, most of the study areas are recovered well, meaning structure on the order of $0.2°$ (about 20 km) or larger can be recovered in our model. This is a vast improvement on past studies (e.g. Fu et al., 2016; Kim et al., 2017; Zhu et al., 2019; Fan et al., 2021; Li et al., 2022; Figure S6; Table S4), where the minimum size of anomalous body structure that can be resolved is $1° - 1.5°$ (about 100 - 150 km). The model in the north is not well recovered owing to the poor path coverage at a period of 3 s, but the crust beneath CBVF, the main focus of this study, is better recovered as this is where the station distribution is densest.

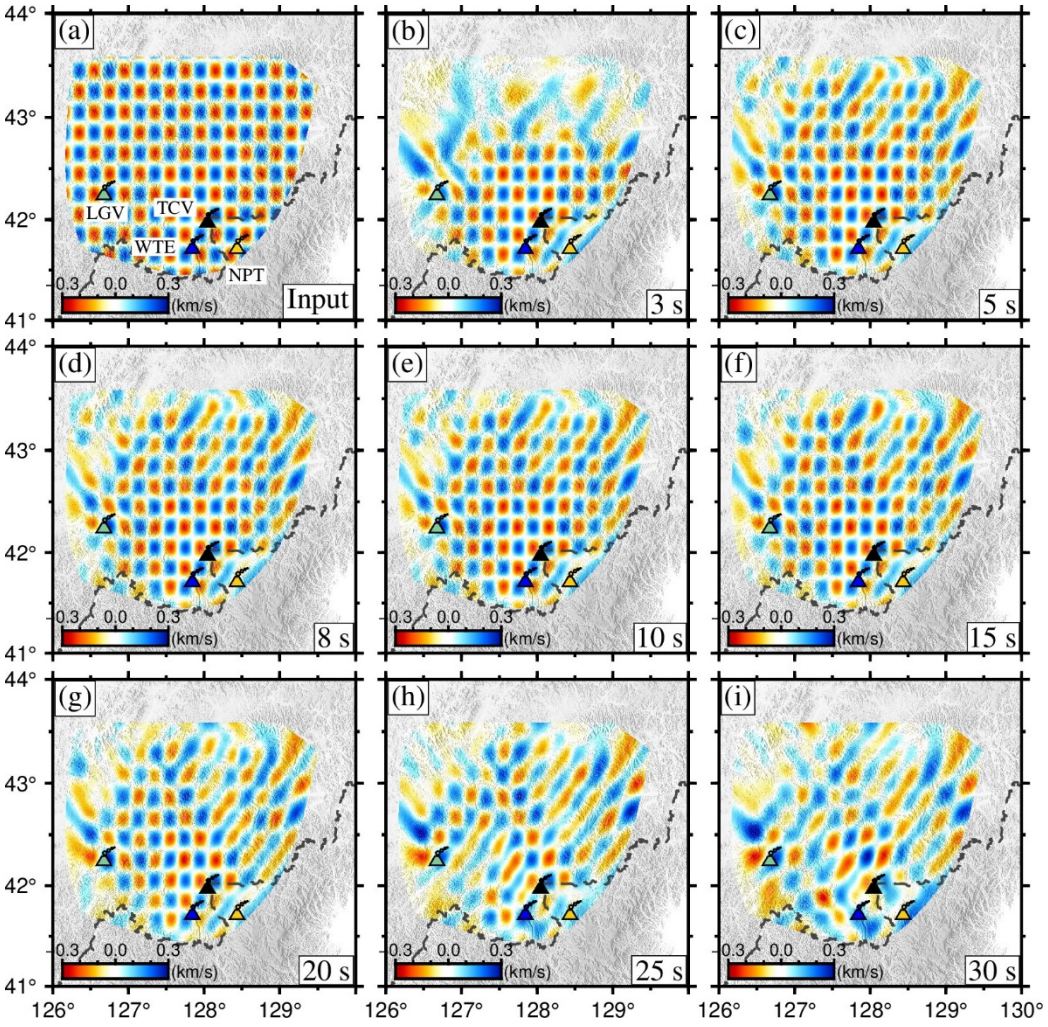


**Figure 4**

### 3.2 Phase velocity maps

We obtained Rayleigh wave phase velocity tomography with an interval of 1 s at periods of 2-37 s. The velocity anomalies are calculated relative to the average phase velocity for each period of the study area. Figure 5 a-d show examples of phase velocity maps at 3, 5, 8 and 10 s periods, where Rayleigh wave is sensitive to structures in the upper crust (Figure S7). As shown in Figure 5, TCV shows a significant low velocity anomaly, the velocity beneath WTE and NPT is close to the background velocity, whereas the Longgang volcano (LGV) is characterized by weak high velocity anomaly. Our model shows more detailed structures compared with previous study (Figure S7)

Figure 5 e-h show phase velocity maps at 15, 20, 25 and 30 s periods, where Rayleigh waves are sensitive to structures in the middle-lower crust (Figure S8). At periods of 15 s and 20 s, TCV shows limited low velocities compared with the surrounding region, the velocity beneath the LGV is close to background velocity. At 25 s and 30 s periods, low velocities are observed in the south of 43°N and significant high velocity is present north of 43°N. The crust beneath TCV shows low velocities, while the velocities beneath WTE and NPT are close to background velocities.

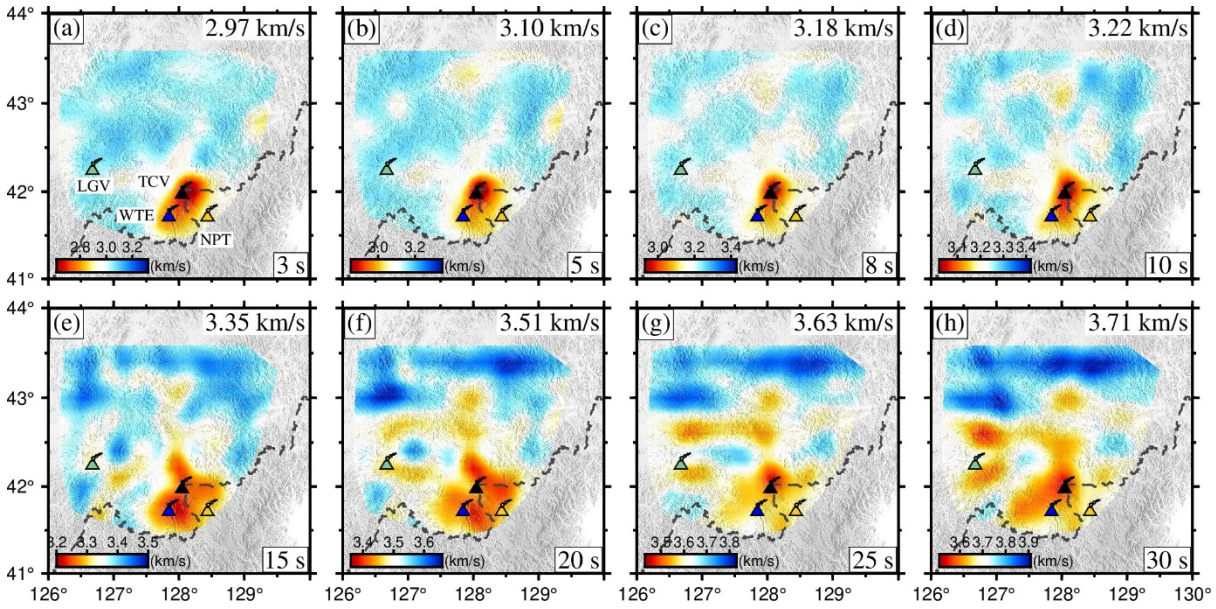


**Figure 5**

### 3.3 Shear wave velocity

The joint inversion results for receiver functions and surface waves show striking similarities (Figure 6) to the inversion of the ambient noise alone. All Rayleigh wave dispersion curves are fit well, and Moho related phases of RFs are also fit well. Observed RFs are more complicated at stations close to TCV, with some signal in the first 2 s not matched well. Interestingly, past RFs studies show evidence for azimuthal variations in transverse and radial RFs, interpreted as dipping layers (Hammond et al., 2020). This may explain our poor fits to our stacked RFs. As before, our 1D profiles reveal two low Vs anomalies below the TCV, while the velocities beneath WTE and NPT are close to normal upper crust.

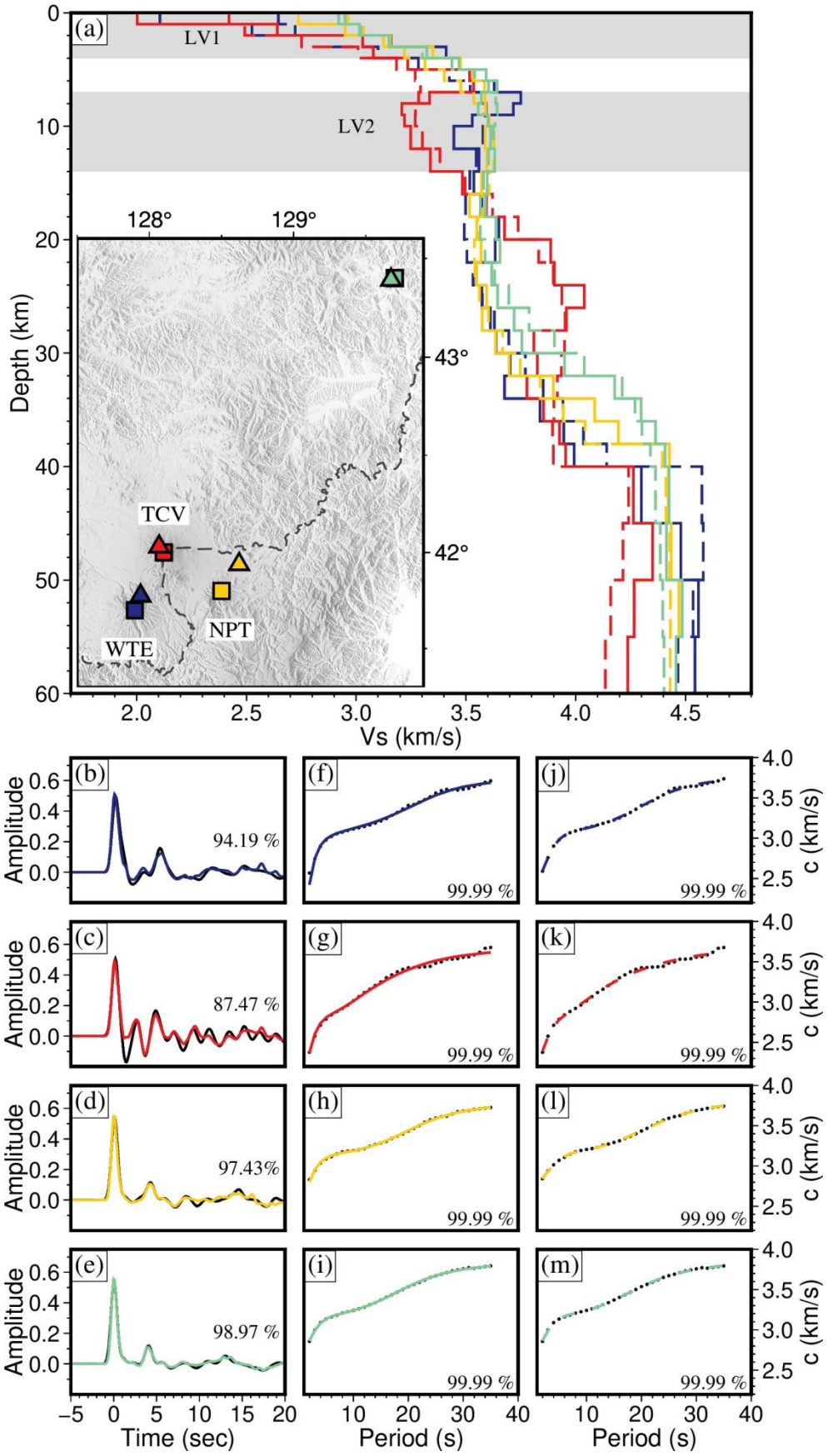
(a)
LV1
LV2
128°
129°
43°
42°
TCV
NPT
WTE
Depth (km)
Vs (km/s)
(b)
(c)
(d)
(e)
(f)
(g)
(h)
(i)
(j)
(k)
(l)
(m)
94.19 %
87.47 %
97.43%
98.97 %
99.99 %
Amplitude
c (km/s)
Time (sec)
Period (s)
Period (s)

**Figure 6**

RFs have sensitivity to the crust directly beneath a seismic station. This means that we generate an incomplete lateral coverage for the joint inversion, precluding a robust 3D joint model. Rather, we plot the results of joint inversion (Figures 7a'-f') on the horizontal slices of ANT (Figures 7a-f) where they show striking similarities to the ambient noise models, but with extra detail on velocity discontinuities. Figure 7 shows a series of horizontal slices of the ANT and joint inversion model at 6 depths from 2 km to 50km. To better visualize the vertical structure below the CBVF, we plot four profiles across the TCV, WTE and NPT in Figure 8. In the shallow crust (Figures 7a, a' and 8), TCV shows significant low velocity, the velocity perturbation is > 15% (black dotted line in Figures 7a, a' and white solid line in Figure 8) and the surrounding region shows relatively high Vs structures. At a depth of 6 km, TCV shows a local low velocity structure compared with WTE and NPT. In the upper crust (Figures 7c, c' and 8), a significant low velocity zone is visible beneath TCV, suggesting a magma reservoir exists at this depth. However, WTE and NPT show high velocity structures. At a depth of 25 km, TCV shows a relatively high velocity anomaly compared to WTE and NPT. Previous studies (Kim et al., 2017; Zhu et al., 2019) also revealed a relatively high velocity structure at this depth. At the bottom of the crust and the uppermost mantle (Figures 7e, e', f, f' and 8), low velocity anomalies exist beneath the TCV. These are consistent with those of recent studies (Fan and Chen, 2019; Zhu et al., 2019; Fan et al., 2021, Fig S7).

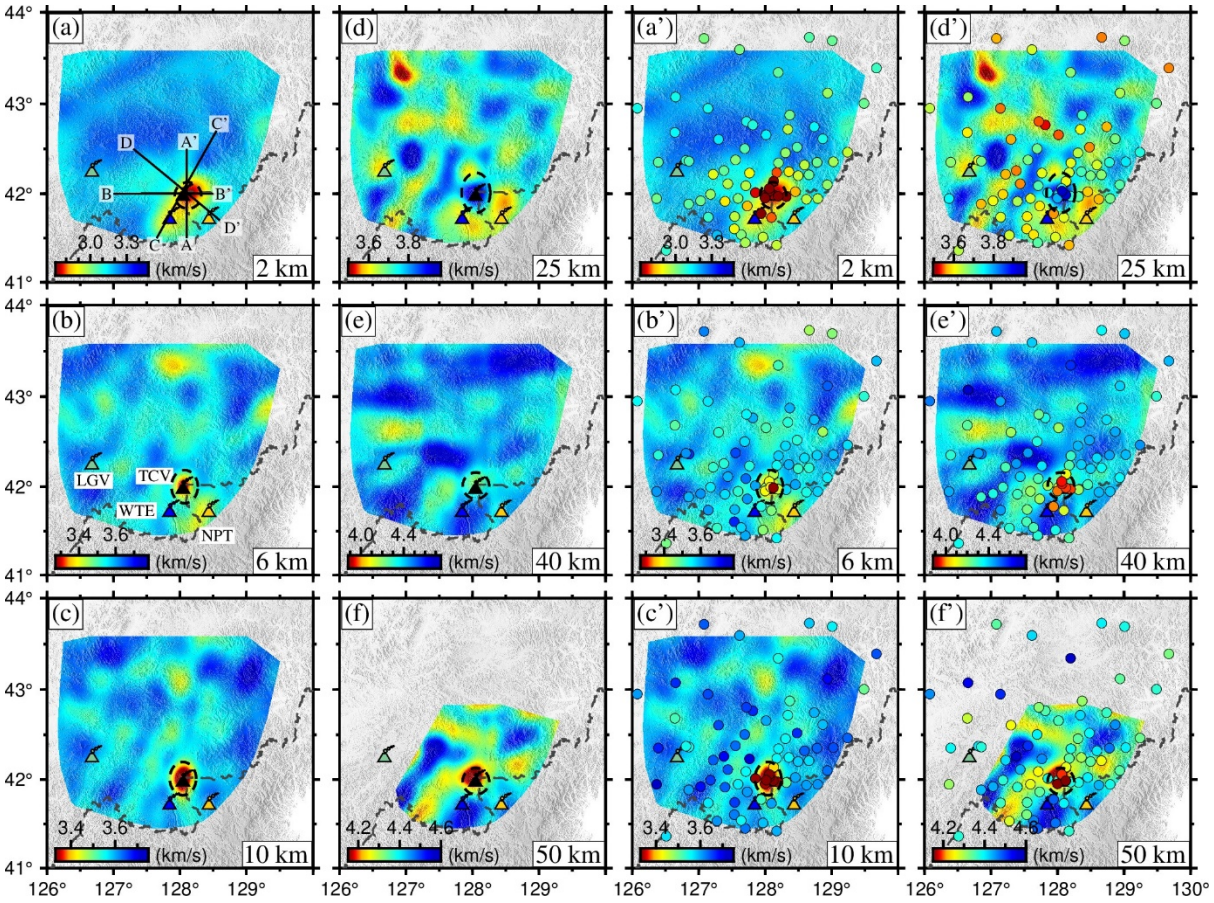


**Figure 7**

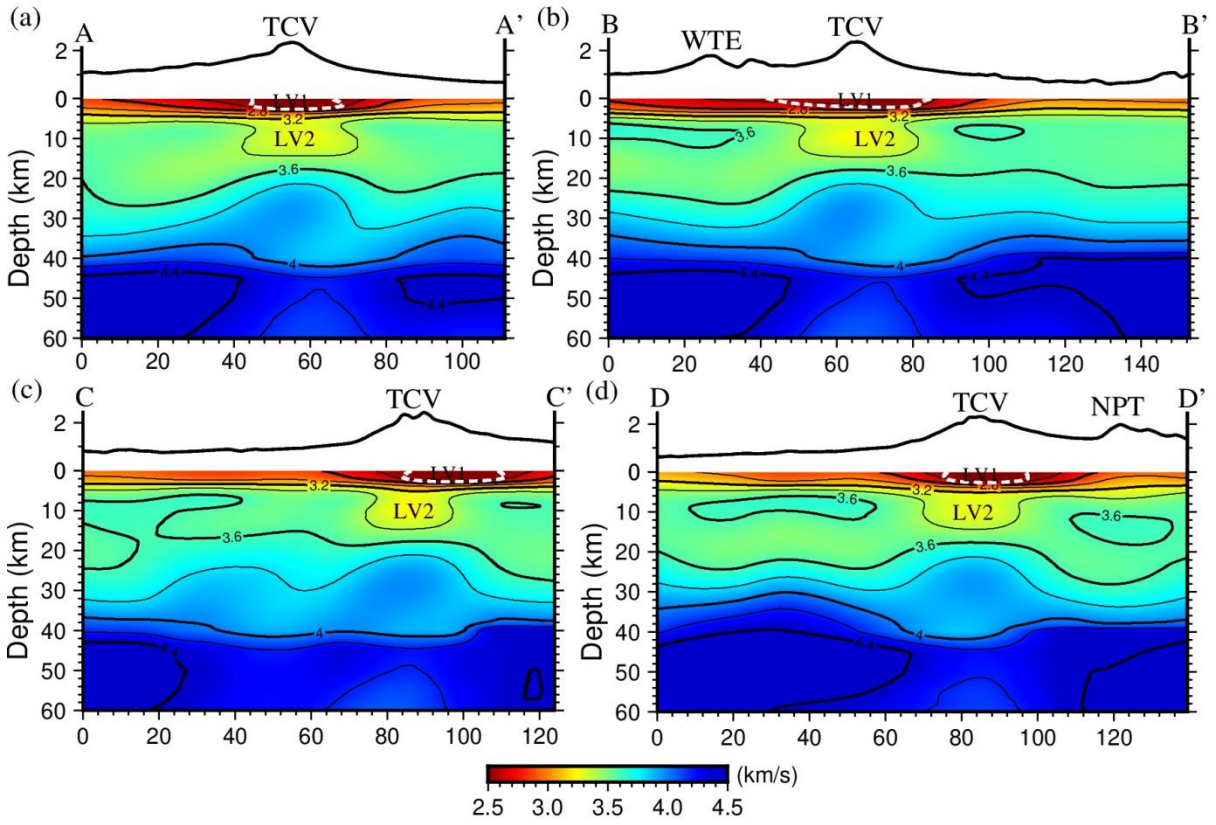


**Figure 8**

## 4 Estimating melt fractions

In this study, we estimate melt fractions at 0-4 km and 7-14 km beneath TCV basing on the shear wave velocity anomalies from this study and resistivity anomalies from previous studies (Qiu et al., 2018, Yang et al., 2021). We follow the method of Yang et al. (2021) to estimate melt fractions associated with the resistivity measurements. Namely, a modified Archie's Law (Glover et al., 2000), with varying cementation factors (m) to represent connected (m = 1) versus isolated pores (m = 2) and also the Hashin-Shtrikman higher-conductivity bound (Hashin and Shtrikman, 1963). For the rock and melt properties, we use those defined in Yang et al., 2021 (Table S3). Modelling of the MT data alone gives a range of melt fractions of 5-24% (Qiu et al., 2018), 7-30% (Yang et al., 2021) at 0-4 km and 2-17% (Qiu et al., 2018), 7-30% (Yang et al., 2021) at 7-14 km.

We use two methods to estimate melt fractions from the seismic data estimated from our joint inversions. First, we follow the theory proposed by Tandon and Weng (1984) to calculate elastic constants and aggregate density, which is based on the assumption that an applied stress is perturbed by inclusions. For these models, we can control the shape of the inclusions, ranging from low aspect ratio ($\alpha$) penny shaped inclusions ($\alpha << 1$), through spherical inclusions ($\alpha = 1$) to elongated, cigar shaped inclusions ($\alpha >> 1$). Table S4 gives parameters used in the models. Here, we set the aspect ratio to 0.05-0.2, a range proposed for melts in textural equilibrium (Takei, 2002). We take the matrix velocities from the joint RFs inversions away from TVC as representative of the rock properties. We set the shear-wave

velocity of the melt to 0, and P-wave velocity and density based on estimates for basaltic melt from Clark et al. (2016). Other compositions of melt may change these parameters, but the models are most sensitive to S-wave velocities, which assuming a S-wave velocity of 0 for the melt, is relatively insensitive to changes in composition. However, aspect ratios may change. As our values are quite low, we suggest our estimates are lower bounds for the melt fraction. Modeling of seismic velocities in this way suggests a melt fraction of 18-35% and 2-12% (Figure 9, purple rectangle) is present at 0-4km and 7-14 km depth beneath TCV, respectively.

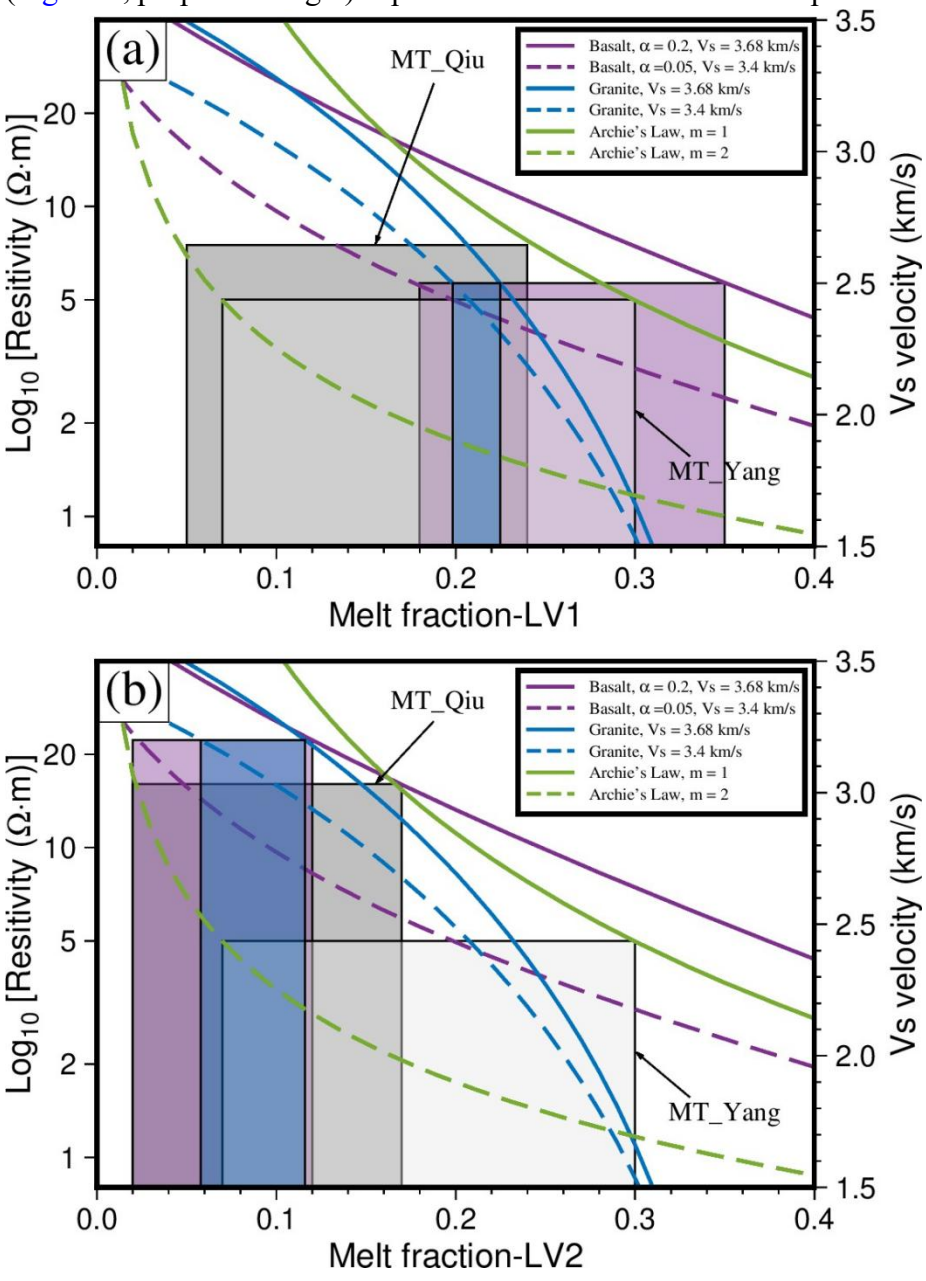


**Figure 9**

Seismic properties vary significantly with the geometric shape of the melt (Hammond & Humphreys, 2000, Hammond & Kendall, 2016, Paulatto et al., 2022), making it extremely complex and prone to large uncertainties when estimating the melt fraction based on seismic velocity. A second method to model melt fractions from seismic velocity has been introduced by Chu et al. (2010) and applied to estimating melt distribution beneath Yellowstone volcano

(Chu et al., 2010), Tengchong volcano (Zhao et al., 2021) and Changbaishan (Zhang, 2023). This method relies on the estimation of the critical porosity, instead of the microgeometry of the melt. We calculated the effective elastic moduli of fluid-saturated porous materials using Gassmann's relations, as follows:

$$M_{eff} = \mu_{dry,} \tag{2}$$

where $\mu_{eff}$ and $\mu_{dry}$ represent the effective shear modulus for the material of the matrix rock and shear modulus of the drained matrix, respectively. For porosity below the critical value,

$$\mu_{dry} = \mu_0 \left(1 - \frac{\emptyset}{\emptyset_c}\right), \tag{3}$$

where $\emptyset_c$ is the critical porosity, $\emptyset$ is the porosity, and $\mu_0$ is the shear modulus for the granite. For granite, laboratory measurement suggests that the critical porosity is 0.35 (van der Molen and Paterson, 1979).

With shear wave velocity $V_s$ and density $\rho_0$ for the granite, $\mu_0$ can be represented as follows,

$$M_0 = V_s^2 \cdot \rho_0, \tag{4}$$

The effective density for the material of the frame rock $\rho_{eff}$ and seismic velocity of the fluid-filled porous material $V_{se}$ can be calculated as follows,

$$P_{eff} = (1 - \emptyset)\rho_0 + \emptyset \sum S_i \rho_I, \tag{5}$$

$$V_{se} = \sqrt{\frac{\mu_{eff}}{\rho_{eff}}}, \tag{6}$$

where $S_i$ and $\rho_i$ are individual fluid saturation and density, respectively.

By using equations (1) - (5), we can get,

$$P_0 V_{se}^2 (1 - \emptyset) + \emptyset \sum S_i \rho_I = V_s^2 \rho_0 \left(1 - \frac{\emptyset}{\emptyset_c}\right), \tag{7}$$

The temperature beneath the TCV is 700-1200 ℃ in the upper crust (Andreeval et al., 2018). And the pressure is 0.1-0.7 GPa (Andreeval et al., 2018; Guo et al., 2015a). Combining equations (6) and parameters in Table S5, we can estimate shear wave velocities for various porosities with different melt and fluid saturations (blue lines in Figure 9). The average velocity in LV1 is 2.5 km/s, which presents ~ 20-22 % melt fractions. A shear wave velocity of 3.2 km/s observed in LV2 is modelled as ~ 6-12 % melt fractions (blue rectangle in Figure 9). It should be noted that melt fraction here could be underestimated. On the one hand, due to the limited sensitivity of seismic waves and the inherent smoothing of many inversion methods, the recovery of low-velocity anomalies is almost always insufficient (Malcolm and Trampert, 2011). On the other hand, estimating the melt fraction by seismically averaging the entire volume of the magma reservoirs will lead to an underestimation of the melt fraction present in sub-seismic wavelength sized features.

## 5 Discussion

The resolution of our new Vs model is ~ 20 km in the upper crust and ~ 30 km in the lower crust (Figures 3, 4). The dominant features of the Vs model are the low Vs anomalies coinciding with the location of TCV in the upper crust (Figures 7, 8). The synthetic restoring test (Figure S10) demonstrated that the low velocity anomalies beneath the CBVF are robustly imaged. In the shallow crust (< 4 km below sea level), the ANT and joint inversion show a strong low velocity zone LV1 beneath TCV (~ 2.5 km/s, Figures 7, 8). This structure shows the lowest velocity in the entire study area. A recent MT study (Yang et al., 2021) detected a low-resistivity body at this depth, which is explained as saline fluids. However, based on melt inclusion studies, this is also the depth suggested for magma reservoirs before the 946 CE eruption (Pan et al., 2007; Yi et al., 2021) and volcano-tectonic seismicity associated with fluid and magma movement occurred within this depth range in 2002-2006 volcanic unrest (Xu et al., 2012), suggesting magma may remain present and/or may have been recharged during the recent unrest. The presence of shallow magma reservoir has also been revealed by previous geophysical studies (e.g., Zhang et al., 2002; Yan et al., 2023). A small-scale magma distribution at depths lower than 8 km just north of TCV was exhibited by results of deep seismic sounding (Zhang et al., 2002), while melting body is suggested at depth of ~5 km beneath and east of TCV by local body-wave tomography (Yan et al., 2023). In comparison, our present model shows the melt resides much shallower and rightly beneath TCV (Figure 8). In the deeper upper crust (~ 7-14 km), the tomographic images show a significant low Vs anomaly (Vs<3.4 km/s, LV2) beneath TCV. The existence of a low velocity zone at these depths is also supported by previous RFs studies (Kyong-Song et al., 2016; Hammond et al., 2020) and joint inversion of ambient noise and RFs (Zhu et al., 2019). The lateral extent of LV2 is ~ 30 km, which is much smaller than previous result of ~100 km (Zhu et al., 2019), due to the improved resolution by using the new datasets (Figures 4, S4, S10). Additionally, a recent thermal structure study (Jiang et al., 2023) showed localized high heat flow value (270±16 $mWm^{-2}$) near the TCV, which suggests the magma is active in the upper crust and the depth of low Vs anomaly is consistent with temperature logging and numerical modeling (Jiang et al., 2023). Effective medium modelling of both MT (Qiu et al., 2018; Yang et al., 2021) and seismic data suggests that this reservoir has relatively low melt fractions (6-12%) (Figure 9), but given uncertainties in the relationship between melt properties and seismic velocities (Paulatto et al., 2022), uncertainties are considerable. Further, due to limitations on resolution, we cannot distinguish between high melt fraction lenses on length scales smaller than the seismic resolution or melt distributed throughout the low velocity zone. The distance between TCV and WTE is ~35 km. The structures beneath TCV, WTE and NPT are distinguishable by our new Vs model whereas previous tomographic models couldn't. In stark contrast to TCV, our velocity models include regionally anomalous high velocities at 7-14 km depth beneath WTE and NPT, suggesting that the old magma chambers in upper crust have cooled and that similar storage conditions were present beneath these volcanoes in the past.

The velocity in the middle-lower crust beneath TCV is relatively high compared to the surrounding region (Figures 7, 8). This suggest that not only is there a lack of melt in the lower

crust today, but that the crust has been altered to make it seismically faster. This is as expected for the development of a trans crustal magmatic system, where the injection of sills into the lower crust, and reactive transport of melt to shallow depths results in a high melt fractions layer atop a chemically differentiated lower crust (Jackson et al., 2018). The lateral extent of the high velocity anomaly in the lower crust is ~ 30-40 km, within the resolution of our models (Figure 4), and a vast improvement on past models (Guo et al., 2015b; Kim et al., 2017; Zhu et al., 2017; Fan et al., 2021) where resolution is ~ 100-150 km. This improvement in resolution may explain why our models better support petrological estimates for magma storage beneath TCV. The presence of significant low-velocity anomalies in the shallow crust but not in the deeper crust is also suggested by high-resolution seismic imaging of Long Valley (Jiang et al., 2018), Yellowstone (Jiang et al., 2018), Mount St. Helens (Kiser et al., 2016; 2021), Aso (Abe et al., 2017), Uturuncu/Altiplano Puna (Ward et al., 2014), Colima (Spica et al., 2017) in various tectonic settings, possibly suggesting a common mechanism for magma transport at these large caldera volcanoes.

While we start to lose resolution towards the base of the lower crust and uppermost mantle, our Vs model shows low velocities in the uppermost mantle beneath TCV (Figures 7, 8). A recent MT study (Yang et al., 2021) revealed a low resistivity anomaly in the uppermost mantle beneath TCV, interpreted as the likely source of partial melt that supplies the volcano. The three calderas in CBVF are in close proximity to each other and exhibit comparable magma evolution patterns, bimodal distribution of volcanic rocks, and a mantle source that is enriched (Liu et al., 2015). However, there is limited research on the magma evolution and the temporal and spatial migration of volcanic activity between the three calderas. Our Vs model suggests that the striking differences between the volcanic systems in the crust are also evident in the mantle. A low Vs anomaly exists below TCV at the bottom of the lower crust and uppermost mantle that is not present beneath WTE and NPT. Extending this, large-scale tomography (Wei et al., 2012; Tao et al., 2018; Guo et al., 2018) imaged a low velocity zone at depth ~ 100 km, which is associated with dehydration melting of the Pacific plate. All of this implies that partial melt generated from a localized upwelling beneath CBVF accumulates at the top of the upper mantle, and provides continuous supply for the magma reservoirs in the crust. We propose that magma from the mantle intrudes into the lower-middle crust, where through reactive transport it migrates to form a more evolved upper crustal melt lens beneath CBVF, leaving behind a chemically differentiated crust with faster seismic velocities (Annen et al., 2006, Jackson et al., 2018, Booth et al., 2024). We also suggest that upper crustal low velocities, consistent with depths of more evolved magmas involved in historical eruptions indicate that these may retain some magma or could have been recharged during subsequent unrest, although we cannot distinguish these from the signal of an extensive hydrothermal reservoir. During the unrest from 2002-2005, volcanic earthquakes occurred at a depth of ~ 5 km beneath the TCV suggesting activity in this shallow system (Xu et al., 2012). In contrast, the magma reservoirs beneath WTE and NPT have cooled and the relatively high velocity structures at the bottom of lower crust and uppermost mantle beneath WTE and NPT reflect the lack of magma from the mantle, suggesting these volcanoes lack the potential to erupt in the near future.

## 6 Conclusions

We obtain a high-resolution Vs model of the CBVF magmatic system based on a new dense array and joint ANT and RFs analysis. We found two low velocity zones exist in the upper crust beneath TCV, overlying a faster velocity lower crust (Figure 10). Combing our Vs model with previous geophysical, geochemical and petrological studies, we propose that two magma reservoirs exist below TCV in the upper crust, with migration of magma between the two possibly driving the recent volcanic unrest. Faster upper crustal velocities at similar depths beneath WTE and NPT suggest that similar magmatic systems existed beneath these volcanoes, but they have now frozen.

Similarities beneath TCV to other large caldera volcanoes such as Yellowstone and Long Valley (Jiang et al., 2018) suggests that a mechanism of middle/lower crust magma injection and reactive transport of evolved melts to form an upper crustal melt lens overlying a chemically differentiated crust (e.g., Jackson et al., 2018) is a common mechanism driving large caldera systems.

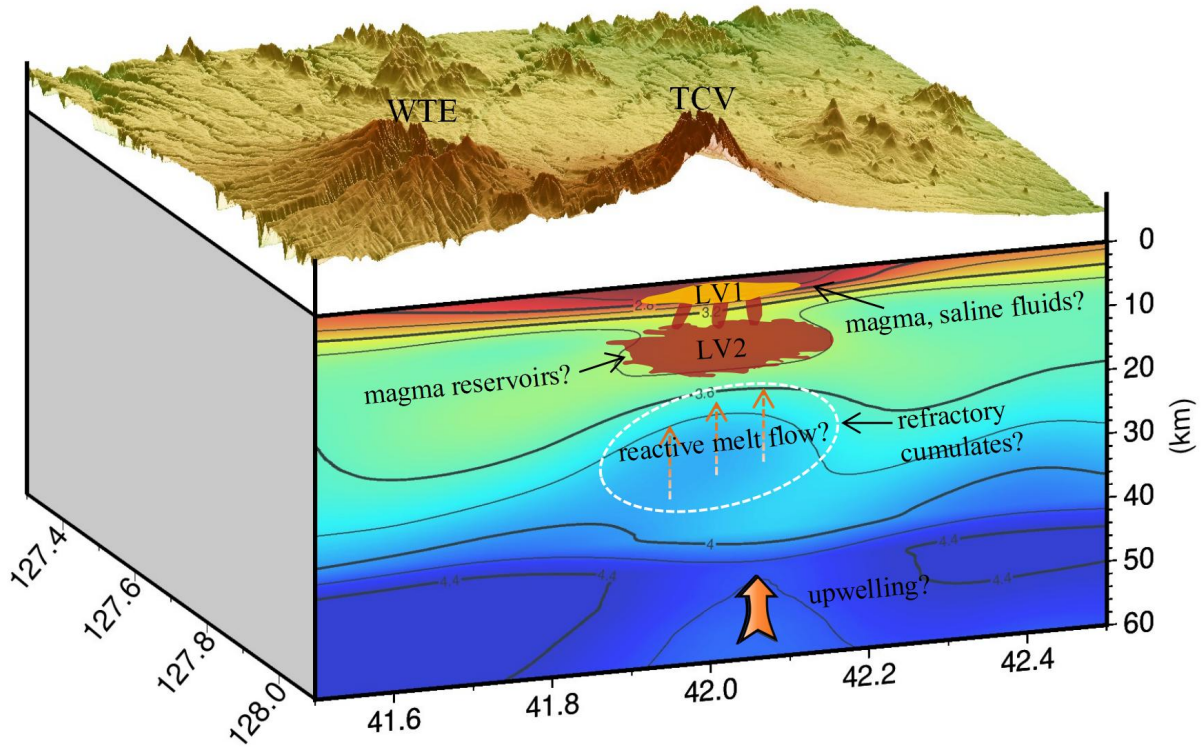


**Figure 10**

## Acknowledgments

This work was supported by Special Fund of State Public Institute for Basic Research (IGCEA1711), National Natural Science Foundation of China (41874110, 42274136, 42072330), and China Scholarship Council (202204190003). Data of the permanent stations

are provided by Data Management Center of China National Seismic Network at Institute of Geophysics, CEA (http://www.seisdmc.ac.cn.) and Jilin Changbaishan Volcano National Observation and Research Station. James Hammond is supported by NERC Knowledge Exchange Fellowship NE/X001717/1 and he and Cunrui Han are supported by grants from the Richard Lounsbery Foundation and the US Government. Data of NECESSarray and DPRK temporary seismic stations are collected from the Incorporated Research Institutions for Seismology (IRIS). We thank Xingli Fan (Fan et al., 2021) for providing access to some Rayleigh wave dispersion data. We also thank Matthew Jackson for discussions on reactive transport of melt in crustal magmatic systems.

## Open Research

Seismic data from the temporary stations of NECESSArray and Mt. Paektu Seismic Network are available at IRIS (https://ds.iris.edu/ds/nodes/dmc/). We thank the Data Management Centre of China National Seismic Network at Institute of Geophysics, China Earthquake Administration, for providing seismic data of permanent stations. We also thank Xingli Fan (Fan et al., 2021) for providing access to some Rayleigh wave dispersion data. Figures were plotted using GMT (Wessel & Smith, 1998 at https://doi.org/10.1029/98EO00426). The results of Vs model and waveforms of permanent stations were available at https://data.mendeley.com/datasets/p932mrfz27/2.

## References

Abe, Y., Ohkura, T., Shibutani, T., Hirahara, K., Yoshikawa, S., & Inoue, H. (2017). Low-velocity zones in the crust beneath Aso caldera, Kyushu, Japan, derived from receiver function analyses. *Journal of Geophysical Research: Solid Earth, 122(3),* 2013–2033. https://doi.org/10.1002/2016JB013686

Andreeva, O. A., Yarmolyuk, V. V., Andreeva, I. A., & Borisovskiy, S. E. (2018). Magmatic evolution of Changbaishan Tianchi Volcano, China-North Korea: evidence from mineralhosted melt and fluid inclusions. *Petrology*, *26*, 515–545, https://doi.org/10.1134/S0869591118050028.

Annen, C., Blundy, J.D., Sparks, & R.S.J. (2006). The genesis of intermediate and silicic magmas in deep crustal hot zones. *Journal of Petrology*, *47*, 505–539, https://doi.org/10.1093/petrology/egi084.

Bensen, G.D., Ritzwoller, M.H., Barmin, M.P., Levshin, A.L., Lin, F., Moschetti, M.P ., Shapiro, N.M., & Yang, Y. (2007). Processing seismic ambient noise data to obtain reliable broad-band surface wave dispersion measurements. *Geophysical Journal International*, *169*, 1239–1260, https://doi.org/10.1111/j.1365-246X.2007.03374.x.

Booth, C. A., Jackson, M. D., Sparks, R. S. J., & Rust, A. C. (2024). Source reservoir controls on the size, frequency, and composition of large-scale volcanic eruptions. Science Advances, 10(19), eadd1595. https://doi.org/10.1126/sciadv.add1595

Brocher, T.M. (2005). Empirical Relations between Elastic Wavespeeds and Density in the Earth's Crust. *Bulletin of the Seismological Society of America*, *95*, 2081–2092,

https://doi.org/10.1785/0120050077.

Chen, S., Lee, S., Simutė, S., Fichtner, A., Lee, T.J., Lee, Y.S., Liu, J., & Gao, R. (2021). Geochemical and seismic tomography constraints of two-layer magma chambers beneath the bimodal volcanism: A case study of late Cenozoic volcanic rocks from Ulleung Island and Mt. Changbai (Paektu). Chemical Geology, 581, 120386, https://doi.org/10.1016/j.chemgeo.2021.120386.

Choi, S.C., Oh, C.W., Götze, & H.J. (2013). Three-dimensional density modeling of the EGM2008 gravity field over the Mount Paekdu volcanic area. Journal of Geophysical Research: Solid Earth, 118, 3820–3836, https://doi.org/10.1002/jgrb.50266.

Chu, R., Helmberger, D.V., Sun, D., Jackson, J.M., & Zhu, L. (2010). Mushy magma beneath Yellowstone. *Geophysical Research Letters*, *37*, https://doi.org/10.1029/2009GL041656.

Crotwell, H. P., Owens, T. J., & Ritsema, J. (1999). The TauP toolkit: Flexible seismic travel-time and ray-path utilities. *Seismological Research Letters*, *70*, 154–160, https://doi.org/10.1785/gssrl.70.2.154.

Fan, Q., Sui, J., Wang, T., Li, N., & Sun, Q. (2007). History of volcanic activity, magma evolution and eruptive mechanisms of the Changbai volcanic province. *Geological Journal of China Universitie*, *13*, 175–190.

Fan, X., Chen, Q., Ai, Y., Chen, L., Jiang, M., Wu, Q., & Guo, Z. (2021). Quaternary sodic and potassic intraplate volcanism in northeast China controlled by the underlying heterogeneous lithospheric structures. *Geology*, *49*, 1260–1264, https://doi.org/10.1130/G48932.1.

Fan, X., Guo, Z., Zhao, Y., & Chen, Q. (2022). Crust and Uppermost Mantle Magma Plumbing System Beneath Changbaishan Intraplate Volcano, China/North Korea, Revealed by Ambient Noise Adjoint Tomography. Geophysical Research Letters, 49, https://doi.org/10.1029/2022GL098308.

Fu, Y.V., Gao, Y., Li, A., Li, L., Shi, Y., & Zhang, Y. (2016). Origin of intraplate volcanism in northeast China from Love wave constraints. *Journal of Geophysical Research: Solid Earth*, *121*, 8099–8112, https://doi.org/10.1002/2016JB013305.

Glover, P.W., Hole, M.J., Pous, J., 2000. A modified Archie's law for two conducting phases. *Earth and Planetary Science Letters*, *180*, 369–383, https://doi.org/10.1016/S0012-821X(00)00168-0.

Guan Y., Choi, S.C., Yang, G., Liu, J., Lee, Y.S., Oh, C.W., Jin, X., & Wu, Y. (2020). Changbaishan Tianchi volcano crustal magma chambers modeling with gravity profile. Acta Petrologica Sinica, 36, 3840–3852, doi: 10.18654/1000-0569/2020.12.16.

Guo, W., Liu, J., Xu, W., Li, W., & Lei, M. (2015a). Reassessment of the magma system beneath Tianchi volcano, Changbaishan: Phase equilibria constraints. *Chinese Science Bulletin*, *60*, 3489–3500, doi: 10.1360/N972015-00487.

Guo, Z., Chen, Y., Ning, J., Feng, Y., Grand, S.P., Niu, F., Kawakatsu, H., Tanaka, S., Obayashi, M., & Ni, J. (2015b). High resolution 3-D crustal structure beneath NE China from joint inversion of ambient noise and receiver functions using NECESSArray data. *Earth and Planetary Science Letters*, *416*, 1–11, https://doi.org/10.1016/j.epsl.2015.01.044.

509 Guo, Z., Wang, K., Yang, Y., Tang, Y., John Chen, Y., & Hung, S. (2018). The Origin and
510 Mantle Dynamics of Quaternary Intraplate Volcanism in Northeast China From Joint
511 Inversion of Surface Wave and Body Wave. *Journal of Geophysical Research: Solid*
512 *Earth*, *123(3)*, 2410–2425. https://doi.org/10.1002/2017JB014948.
513 Hammond, W.C., & Humphreys, E.D. (2000). Upper mantle seismic wave velocity: Effects of
514 realistic partial melt geometries. *Journal of Geophysical Research, 105*, 10975–10986,
515 https://doi.org/10.1029/2000JB900041.
516 Hammond, J.O.S., & Kendall, J.-M. (2016). Constraints on melt distribution from seismology:
517 a case study in Ethiopia. *Geological Society, London, Special Publications*, *420*, 127–147.
518 https://doi.org/10.1144/SP420.14.
519 Hammond, J. O. S., Wu, J., Ri, K. S., Wei, W., Yu, J., & Oppenheimer, C. (2020). Distribution
520 of partial melt beneath Changbaishan/Paektu volcano, China/Democratic People's
521 Republic of Korea. *Geochemistry, Geophysics, Geosystems*, *21*, e2019GC008461,
522 https://doi.org/10.1029/2019GC008461.
523 Han, C., Hammond, J.O.S., Ballmer, M.D., Wei, W., Xu, M., Huang, Z., & Wang, L. (2024).
524 Multi-scale anisotropy in NE China: Evidence for localized mantle upwelling. *Earth and*
525 *Planetary Science Letter*s, *625*, 118495, https://doi.org/10.1016/j.epsl.2023.118495.
526 Hashin, Z., & Shtrikman, S. (1963). A variational approach to the theory of the elastic
527 behaviour of multiphase materials. *Journal of the Mechanics and Physics of Soli*ds, *11(2)*,
528 127–140, https://doi.org/10.1016/0022-5096(63)90060-7.
529 Herrmann, R.B. (2013). Computer programs in seismology: an evolving tool for instruction
530 and research. *Seismological Research Letters*, *84 (6)*, 1081–1088.
531 https://doi.org/10.1785/0220110096.
532 Iacovino, K., Ju-Song, K., Sisson, T., Lowenstern, J., Kuk-Hun, R., Jong-Nam, J., Kun-Ho, S.,
533 Song-Hwan, H., Oppenheimer, C., Hammond, J.O.S., Donovan, A., Liu, K.W., & Kum-
534 Ran, R. (2016). Quantifying gas emissions from the “Millennium Eruption” of Paektu
535 volcano, Democratic People’s Republic of Korea/China. Science Advances, 2, e1600913,
536 doi:10.1126/sciadv.1600913.
537 Jackson, M.D., Blundy, J. & Sparks, R.S.J. (2018). Chemical differentiation, cold storage and
538 remobilization of magma in the Earth’s crust. *Nature*. *564*, 405–409,
539 https://doi.org/10.1038/s41586-018-0746-2.
540 Jiang, G., Hu, S., Cui, T., Qian, C., Liu, F., Zhang, C., Wang, Z., Wang, Y., Hou, T., & Tian,
541 Y. (2023). Thermal structure beneath Changbaishan Volcano, northeastern Asia: new
542 insights from temperature logging and numerical modelling. *Geophysical Journal*
543 *International*, *235*, 1228–1239, https://doi.org/10.1093/gji/ggad300.
544 Julia, J., Ammon, C.J., Herrmann, R.B. & Correig, A.M. (2000). Joint inversion of receiver
545 function and surface wave dispersion observations. *Geophysical Journal International*,
546 *143*, 99–112, https://doi.org/10.1046/j.1365-246x.2000.00217.x.
547 Kim, S., Tkalčić, H., & Rhie, J. (2017). Seismic constraints on magma evolution beneath
548 Mount Baekdu (Changbai) volcano from transdimensional Bayesian inversion of ambient
549 noise data: Magmatic Structure Beneath Mount Baekdu Volcano. *Journal of Geophysical*
550 *Research: Solid Earth*, *122*, 5452–5473, https://doi.org/10.1002/2017JB014105.

Kiser, E., Palomeras, I., Levander, A., Zelt, C., Harder, S., Schmandt, B., et al. (2016). Magma reservoirs from the upper crust to the Moho inferred from high-resolution Vp and Vs models beneath Mount St. Helens, Washington State, USA. *Geology, 44(6),* 411–414. https://doi.org/10.1130/G37591.1.

Kiser, E., Levander, A., Schmandt, B., & Hansen, S. (2021). Seismic Evidence of Bottom-Up Crustal Control on Volcanism and Magma Storage Near Mount St. Helens. *Geophysical Research Letters, 48(5)*, e2020GL090612. https://doi.org/10.1029/2020GL090612.

Kyong-Song, R., Hammond, J. O. S., Chol-Nam, K., Hyok, K., Yong-Gun, Y., Gil-Jong, P., Chong-Song, R., Oppenheimer, C. Liu, K, W., Iacovino, K., & Kum-Ran, R. (2016). Evidence for partial melt in the crust beneath Mt. Paektu (Changbaishan), Democratic People's Republic of Korea and China. *Science Advances*, *2*, e1501513, https://doi.org/10.1126/sciadv.1501513.

Lee, S.H., Oh, C.W., Lee, Y.S., Lee, S.G., & Liu, J. (2021). Petrogenesis of the Cenozoic volcanic rocks in Baekdu volcano in northeastern Asia and the expected depth of the magma chamber based on geochemistry, mineral chemistry, and Sr-Nd-Pb isotope chemistry. Lithos, 388–389, 106080, https://doi.org/10.1016/j.lithos.2021.106080.

Lei, J., & Zhao, D. (2005). P-wave tomography and origin of the Changbai intraplate volcano in Northeast Asia. *Tectonophysics*, *397*, 281–295, https://doi.org/10.1016/j.tecto.2004.12.009.

Levshin, A.L., & Ritzwoller, M.H. (2001). Automated detection, extraction, and measurement of regional surface waves. *Pure and Applied Geophysics*, *158*, 1531–1545, https://doi.org/10.1007/Pl00001233.

Li, H, Tian, Y., Zhao, D, Kumar, R., Li, H, Yan, D., & Liu, C. (2022). Shear-wave tomography of the Changbai volcanic area in NE China derived from ambient noise and seismic surface waves. *Journal of Asian Earth Sciences*, *258*, 105482, https://doi.org/10.1016/j.jseaes.2022.105482.

Ligorría, J. P., & Ammon, C. J. (1999). Iterative deconvolution and receiver-function estimation. *Bulletin of the Seismological Society of Amer*ica, *89(5)*, 1395–1400, https://doi.org/10.1785/BSSA0890051395.

Liu, G., Yang, J., Wang, L., & Sun, J. (2011). Active level analysis of the Tianchi volcano in Changbaishan, China. Bulletin of Mineralogy, *Petrology and Geochemistry*, *30*, 393–399.

Liu, J., Chen, S., Guo, Z., Guo, W., He, H., You, H., Kim, H.M., Sung, G., & Kim, H. (2015). Geological background and geodynamic mechanism of Mt. Changbai volcanoes on the China-Korea border. *Lithos*, *236–237*, 46–73, https://doi.org/10.1016/j.lithos.2015.08.011.

Malcolm, A. E., & Trampert, J. (2011). Tomographic errors from wave front healing: More than just a fast bias. *Geophysical Journal International*, *185*, 385–402, https://doi.org/10.1111/j.1365-246X.2011.04945.x

Oppenheimer, C., Wacker, L., Xu, J., Galvan, J.D., Stoffel, M., Guillet, S., et al. (2017). Multi-proxy dating the 'Millennium Eruption' of Changbaishan to late 946 CE. *Quaternary Science Reviews*, *158*, 164–171, https://doi.org/10.1016/j.quascirev.2016.12.024.

Paulatto, M., Hooft, E.E., Chrapkiewicz, K., Heath, B., Toomey, D.R. & Morgan, J.V. (2022).

593 Advances in seismic imaging of magma and crystal mush. *Frontiers in Earth Science*, *10*,
594 970131, https://doi.org/10.3389/feart.2022.970131.
595 Pan, B., de Silva, S.L., Xu, J., Chen, Z., Miggins, D.P., & Wei, H. (2017). The VEI-7
596 Millennium eruption, Changbaishan-Tianchi volcano, China/DPRK: New field,
597 petrological, chemical constraints on stratigraphy, volcanology, and magma dynamics.
598 *Journal of Volcanology and Gethermal Research*, *343*, 45–59,
599 https://doi.org/10.1016/j.jvolgeores.2017.05.029.
600 Qiu, G., Fang, H., Zhang, J., Pei, F., Lv, Q.Y., & Peng, Y. (2018). Electrical Resistivity
601 Structure of Changbai Volcanic Mountain: Results from Magnetotelluric Exploration
602 Methods. *In Proceedings of the International Workshop on Environment and Geoscience*,
603 344–352.
604 Rawlinson, N., & Sambridge, M. (2005). The fast marching method: An effective tool for
605 tomographic imaging and tracking multiple phases in complex layered media. *Exploration*
606 *Geophysics*, *36*, 341–350, https://doi.org/10.1071/EG05341.
607 Ruan S., Tang J., Dong Z., Wang L., Deng Y., & Han B. (2020). Electric structure model of
608 Tianchi vlocano in Changbai mountain based on three-dimensional AR-QN
609 magnetotelluric inversion. Seismology and geology, 42, 1282–1300,
610 https://www.dzdz.ac.cn/CN/Y2020/V42/I6/1282.
611 Sethian, J. A. (1996). A fast marching level set method for monotonically advancing fronts.
612 *Proceedings of the National Academy of Sciences*, *93*, 1591–1595,
613 https://doi.org/10.1073/pnas.93.4.159.
614 Shen, W., Ritzwoller, M.H., Kang, D., Kim, Y.H., Lin, F., Ning, J., Wang, W., Zheng, Y., &
615 Zhou, L. (2016). A seismic reference model for the crust and uppermost mantle beneath
616 China from surface wave dispersion. *Geophysical Journal International*, *206*, 954–979,
617 https://doi.org/10.1093/gji/ggw175.
618 Song, J., Hetland, E.A., Wu, F., Zhang, X., Liu, G., & Yang, Z. (2007). P-wave velocity
619 structure under the Changbaishan volcanic region, NE China, from wide-angle reflection
620 and refraction data. Tectonophysics, 433, 127–139,
621 https://doi.org/10.1016/j.tecto.2006.09.012.
622 Song, X., & Lei, J. (2023). Direct surface-wave tomography under Northeast China: New
623 insights into 3-D crustal S-wave velocity structure and dynamics of intraplate volcanism.
624 Physics of the Earth and Planetary Interiors, 334, 106959,
625 https://doi.org/10.1016/j.pepi.2022.106959.
626 Spica, Z., Perton, M., & Legrand, D. (2017). Anatomy of the Colima volcano magmatic system,
627 Mexico. Earth and Planetary Science Letters, 459, 1–13.
628 https://doi.org/10.1016/j.epsl.2016.11.010.
629 Sun, C., Plunkett, G., Liu, J., Zhao, H., Sigl, M., McConnell, J.R., Pilcher, J.R., Vinther, B.,
630 Steffensen, J.P., & Hall, V. (2014). Ash from Changbaishan millennium eruption recorded
631 in Greenland ice: Implications for determining the eruption's timing and impact.
632 *Geophysical Research Letters*, *41*, 694–701, https://doi.org /10.1002/2013GL058642.
633 Tandon, G.P., & Weng, G. (1984). The effect of aspect ratio of inclusions on the elastic
634 properties of unidirectionally aligned composites. *Polymer Composites*, *5*, 327–333,

https://doi.org/10.1002/pc.750050413.

Tang, J., Liu, T., Jiang, Z., Zhao, G., Wang, J., & Zhan, Y. (1997). Preliminary observations of the Tianchi volcano area in Changbaishan mountain by mt method. *Seismology and Geology*, *19*, 164–170.

Tang, J., Deng, Q., Zhao, G., Li, W., Xuan, F., Jin, G., Bai, D., Zhan, Y., Liang, J., Pu, X., Wang, J., Li, G., Hong, F., Ma, M., & Chen, F. (2001). Electric conductivity and magma chamber at the Tianchi volcano area in Changbaishan Mountain. Seismology and Geology, 23, 191–200.

Tang, Y., Obayashi, M., Niu, F., Grand, S.P., Chen, Y., Kawakatsu, H., Tanaka, S., Ning J., & James F.N. (2014). Changbaishan volcanism in northeast China linked to subduction-induced mantle upwelling. *Nature Geoscience*, *7*, 470–475, https://doi.org/10.1038/ngeo2166.

Tao, K., Grand, S. P., & Niu, F. (2018). Seismic Structure of the Upper Mantle Beneath Eastern Asia From Full Waveform Seismic Tomography. *Geochemistry, Geophysics, Geosystems*, 19(8), 2732–2763, https://doi.org/10.1029/2018GC007460.

Ward, K. M., Zandt, G., Beck, S. L., Christensen, D. H., & McFarlin, H. (2014). Seismic imaging of the magmatic underpinnings beneath the Altiplano-Puna volcanic complex from the joint inversion of surface wave dispersion and receiver functions. *Earth and Planetary Science Letters, 404,* 43–53. https://doi.org/10.1016/j.epsl.2014.07.022.

Wei, H., Liu, G., & Gill, J. (2013). Review of eruptive activity at Tianchi volcano, Changbaishan, northeast China: Implications for possible future eruptions. *Bulletin of Volcanology*, *75*, 1–14, https://doi.org/10.1007/s00445-013-0706-5.

Wei, W., Xu, J., Zhao, D., & Shi, Y. (2012). East Asia mantle tomography: New insight into plate subduction and intraplate volcanism. *Journal of Asian Earth Sciences*, 60, 88–103, https://doi.org/10.1016/j.jseaes.2012.08.001.

Wu, J., Ming, Y., Zhang H., Su, W., & Liu, Y. (2005). Seismic activity at the changbaishan tianchi volcano in the summer of 2002. *Chinese Journal of Geophysics*, *48*, 621–628.

Wu, J., Ming, Y., Fang, L., & Wang, W. (2009). S-wave velocity structure beneath Changbaishan volcano inferred from receiver function. Earthquake Science, 22, 409–416, https://doi.org/10.1007/s11589-009-0409-3.

Xu, J., Liu, G., Wu, J., Ming, Y., Wang, Q., Cui, D., Shangguan, Z., Pan, Bo., Lin, X., & Liu, J. (2012). Recent unrest of Changbaishan volcano, northeast China: A precursor of a future eruption?. *Geophysical Research Letters*, *39*, https://doi.org/10.1029/2012GL052600.

Xu, J., Pan, B., Liu, T., Hajdas, I., Zhao, B., Yu, H., Liu, R., & Zhao, P. (2013). Climatic impact of the Millennium eruption of Changbaishan volcano in China: New insights from high-precision radiocarbon wiggle-match dating. *Geophysical Research Letter*s, *40*, 54–59, https://doi.org/10.1029/2012GL054246.

Yan, D., Tian, Y., Zhao, D., & Li, H. (2023). Seismicity and magmatic system of the Changbaishan intraplate volcano in East Asia. *Journal of Geophysical Research: Solid Earth, 128,* e2023JB026853. https://doi.org/10.1029/2023JB026853.

Yang, B., Lin, W., Hu, X., Fang, H., Qiu, G., & Wang, G. (2021). The magma system beneath

Changbaishan-Tianchi Volcano, China/North Korea: Constraints from three-dimensional magnetotelluric imaging. *Journal of Volcanology and Gethermal Research*, *419*, https://doi.org/10.1016/j.jvolgeores.2021.107385.

Yi, J., Wang, P., Shan, X., Ventura, G., Wu, C., Guo, J., Liu, P., & Li, J. (2021). Modeling the multi-level plumbing system of the Changbaishan caldera from geochemical, mineralogical, Sr-Nd isotopic and integrated geophysical data. *Geoscience Frontiers*, *12*, 101171, https://doi.org/10.1016/j.gsf.2021.101171.

Zhang, H. (2023). Shallow Magmatic System of the Changbai Volcano Revealed by Ambient Noise Tomography with a Dense Array [Ph.D. thesis]. Jilin University, P631.4.

Zhang, X., Zhang, C., Zhao, J., Yang, Z., Li, S., Zhang, J., Liu, B., Cheng, S., Sun, G., & Pan, S. (2002). Deep seismic sounding investigation into the deep structure of the magma system in Changbaishan-Tianchi volcanic region. Acta Seismologica Sinica, 15, 143–151, https://doi.org/10.1007/s11589-002-0003-4.

Zhao, D., Tian, Y., Lei, J., Liu, L., & Zheng, S. (2009). Seismic image and origin of the Changbai intraplate volcano in East Asia: Role of big mantle wedge above the stagnant Pacific slab. *Physics of the Earth and Planetary Interiors*, *173(3-4)*, 197–206, https://doi.org/10.1016/j.pepi.2008.11.009.

Zhao, D., & Tian, Y. (2013). Changbai intraplate volcanism and deep earthquakes in East Asia: a possible link?. *Geophysical Journal International*, *195*, 706–724, https://doi.org/10.1093/gji/ggt289.

Zhao, Y., Guo, Z., Wang, K., & Yang, Y. (2021). A Large Magma Reservoir Beneath the Tengchong Volcano Revealed by Ambient Noise Adjoint Tomography. *Journal of Geophysical Research: Solid Earth*, *126*, e2021JB022116, doi:10.1029/2021JB022116.

Zhu, H., Tian, Y., Zhao, D., Li, H., & Liu, C. (2019). Seismic Structure of the Changbai Intraplate Volcano in NE China From Joint Inversion of Ambient Noise and Receiver Functions. *Journal of Geophysical Research: Solid Earth*, *124*, 4984–5002, https://doi.org/10.1029/2018JB016600.

**Figure 1.** (a) Topographic map of Northeast China and adjacent areas. The red rectangle shows the present study region. The red triangles show the Holocene volcanic fields. ABG-Abaga, CBVF-Changbaishan volcanic field, HLH-Halaha, JPH-Jingpohu, LG-Longgang, WDLC-Wudalianchi. The blue and red dashed lines show the Tanlu fault and North-south gravity lineament, respectively. And the black dashed lines denote the isodepth contours of the subducting Pacific plate, the yellow arrow denotes the westward subduction of Pacific plate. (b) Seismic stations distribution used in this study. See key for details on the seismic networks. The black dashed lines denote the three calderas in CBVF. For detail about stations see Table S1 in the Supplemental Material.

**Figure 2.** Magma reservoirs/storage depths proposed in previous studies.

**Figure 3.** (a), (b) and (c) are partial folded Green's functions used in this study. Waveforms of Rayleigh wave (Z-Z component) were filtered at three period bands of 5-10 s, 10-20 s and 20-

35 s, respectively. The right panel in each figure shows the associated histograms of the number of CCFs at different inter-station distances for 10 km bins.

**Figure 4.** Checkboard test with a cell size of $0.2° \times 0.2°$ used to evaluate the resolution of the data at different periods. (a) Input model consisting of velocity anomalies of $\pm 0.3\ km/s$ with respect to the mean velocity. (b-i) Recovered models at periods of 3, 5, 8, 10, 15, 20, 25 and 30 s, respectively. The black volcano symbols denote intraplate volcanoes with the location shown in Figure 1a.

**Figure 5.** Phase velocity maps at 3-30 s periods. In each panel, the period, average phase velocity and colorbar are labeled at the at the bottom-right, top-right and bottom-left, respectively. The black volcano symbols mark the intraplate volcanoes (TCV, WTE, NPT, and LGV) shown in Figure 1a.

**Figure 6.** (a) 1D profiles of joint inversion and ANT. The locations of joint inversion (triangles) and ANT (squares) are in the inset map. Dashed lines show ANT inversion only and solid lines show joint inversion velocity profiles. (b-e) Colored lines denote predicted RFs derived from inverted velocity models of joint inversion. The black line denotes observed RFs. (f-i) Colored lines denote the predicted phase velocity dispersion from inverted velocity models of joint inversion. Black dots represent the observed phase velocity dispersion. (j-m) Colored dotted lines denote the predicted phase velocity dispersion from inverted velocity models of ANT grids. Black dots represent the observed phase velocity dispersion.

**Figure 7.** Depth slices of the Vs model. a-f, Vs inverted by ANT. a'-f', the background velocity is inverted by ANT and the circles represent the joint inversion velocities at the same depth. The black volcano symbols mark the intraplate volcanoes shown in Figure 1a. The black and white dotted lines mark the locations of Vs anomaly beneath the TCV and faults, respectively. The colorbar is labeled at the at the bottom.

**Figure 8.** Cross sections of the Vs model, with their locations plotted in Fig. 6a with black solid lines. The colorbar is labeled at the at the bottom. The white dotted lines represent the outline of magma chambers in the shallow crust.

**Figure 9.** (a) The results of melt fractions of LV1 using effective medium modelling. Green lines show how resistivity varies as a function with melt fraction, with grey boxes showing the range of melt fractions predicted by Qiu et al., 2018 and Yang et al., 2021. Purple and green lines show how seismic velocity varies as a function of melt fraction, with purple and blue boxes showing the range of melt fractions predicted by the data. (b) The results of melt fractions of LV2.

**Figure 10.** Cartoon showing the magmatic system beneath CBVF.